Science Advances
AAAS

Supplementary Materials for

Distributed sensing along fibers for smart clothing

Brett C. Hannigan *et al.*

Corresponding author: Brett C. Hannigan, brett.hannigan@hest.ethz.ch; Carlo Menon, carlo.menon@hest.ethz.ch

Sci. Adv. **10**, eadj9708 (2024)
DOI: 10.1126/sciadv.adj9708

This PDF file includes:

S1 Circuit Design Details

We present here a simple, compact, and inexpensive impedance analyzer system that enables distributed sensing on capacitive fibre strain sensors. The system is able to run at high speeds on a low-power commodity field-programmable gate array (FPGA) through a series of hardware optimizations. We reduce digital logic complexity by having the phase-sensitive demodulator (PSD) mixer operate on the single-bit sigma-delta ($\Sigma\Delta$) bistream to eliminate the need for complex multiplier circuits. We use the low-pass nature of the sensor itself to omit the analog reconstruction filter from the digital-to-analog converter (DAC). The $\Sigma\Delta$M design combined with distributed sensing allows reconfigurable time and spatial resolution, by changing the modulator reconstruction filter parameters and excitation frequencies, respectively. The components are described in the Subsections below with reference to Fig. 3d of the main text.

S1.1 Sine Wave Generator

The excitation sine wave generator uses a direct digital synthesis (DDS) approach, as is commonly used in electrical impedance tomography (*44, 45*). A quarter-wave lookup table contains 2^{10} samples of a sine function at 12-bit precision. Symmetry logic allows this table to produce n sine and n cosine signals at frequencies between 1.56 kHz and 99.6 kHz with a time resolution of 157 ns when driven by the 6.375 MHz main sampling clock. It is easily possible to increase the upper frequency limit range by expanding the lookup table. However, the analog front-end currently limits frequency to 100 kHz. The bit depth of the table was chosen from the predicted signal-to-quantization-noise ratio (SQNR) of the DAC, described in Section S1.2. The lookup table (LUT) is based on a multi-port ROM so that sine and cosine waves at multiple frequencies $\{s_i[k], \ldots, s_{N_f}[k], c_i[k], \ldots, c_{N_f}[k]\}$ may be read simultaneously during distributed sensing. Digital sine waves are summed to produce the discrete-time excitation signal $v_{exc}[t]$ that is sent to the DAC. The sine and corresponding cosine signal for each frequency channel

are also forwarded to the PSD through a calibrated delay line (m_i in Fig. 3d of the main text, calibration details described in Section S2) to compensate for the group delay of the analog signal path.

S1.2 Digital-to-Analog Converter

The digital-to-analog converter was designed to minimize the number of analog components. The DAC converts the 16-bit $v_{exc}[t]$ output of the SWG and produces an analog voltage signal $v_{exc}(t)$. The low ratio of maximum SWG output frequency versus system clock frequency motivated our choice of a sigma delta modulator ($\Sigma\Delta$M) DAC architecture. The primary benefit of this architecture are its very low FPGA resource cost of just 129 logic elements and one output pin. We implemented a single-bit, 32 times oversampling $\Sigma\Delta$M with a second order loop filter, which has a known solution for unconditional stability (*46, p. 75*). However, higher order $\Sigma\Delta$M loop filters may be designed with many methods, including some that utilize knowledge of the input signal to improve performance and stability (*47, 48*). We omit the typical analog low-pass reconstruction filter following the modulator to reduce the analog circuit complexity. Instead, we designed the subsequent stages and use the low-pass nature of the sensor itself to perform this filtering without increasing component count. A theoretical SQNR of 70 dB is expected for a $\Sigma\Delta$M of this type (*46, Eq. 3.5*), which has an equivalent number of bits (ENOB) of 11.33, motivating the choice of sine wave sample bit depth discussed above. An SQNR of 58 dB under in-circuit conditions was measured using an oscilloscope FFT function (Fig. S1).

S1.3 Transconductance Amplifier

The PSD impedance analysis technique relies on measurement of voltage $v_{meas}(t)$ across the load under excitation by a known current. The DAC output $v_{exc}(t)$ is a voltage waveform with considerable high-frequency quantization noise introduced by the $\Sigma\Delta$M. This voltage must be

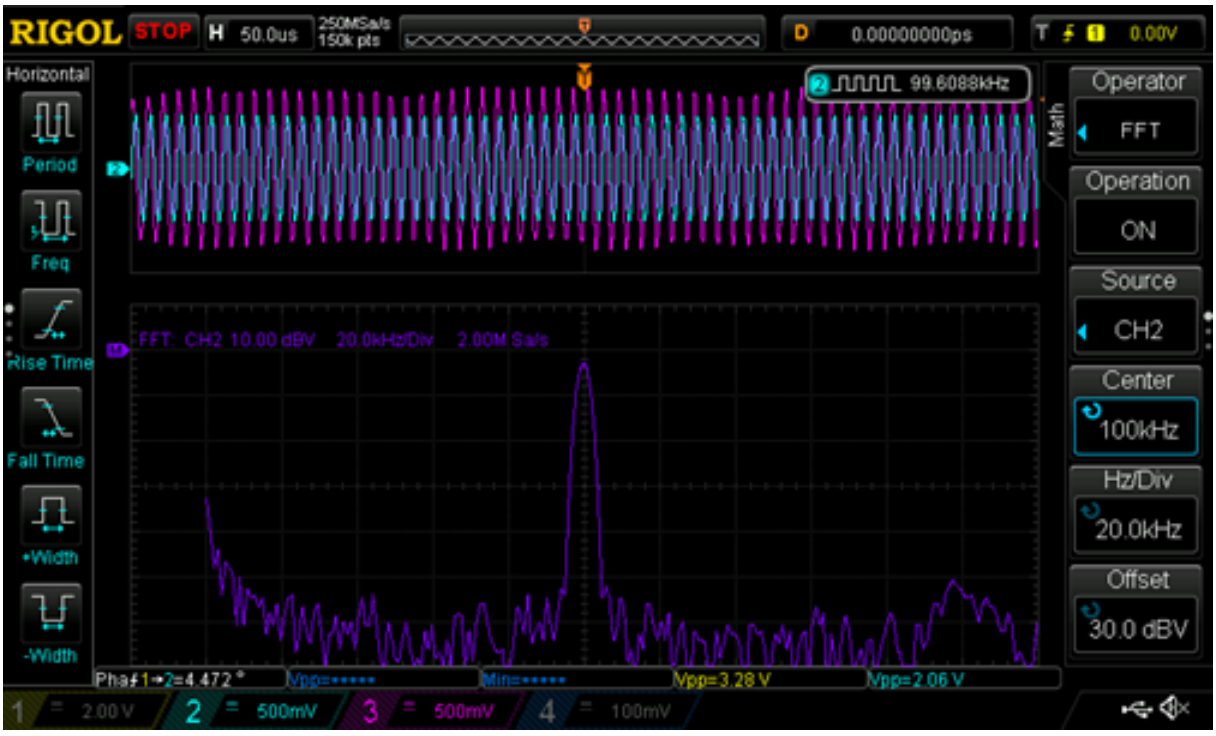

Figure S1: A frequency of 99.6 kHz was output by the SWG (the upper limit of the impedance analyzer design) and used to measure a signal-to-quantization noise ratio (SQNR) of approximately 58 dB and spurious-free dynamic range (SFDR) of 46 dB.

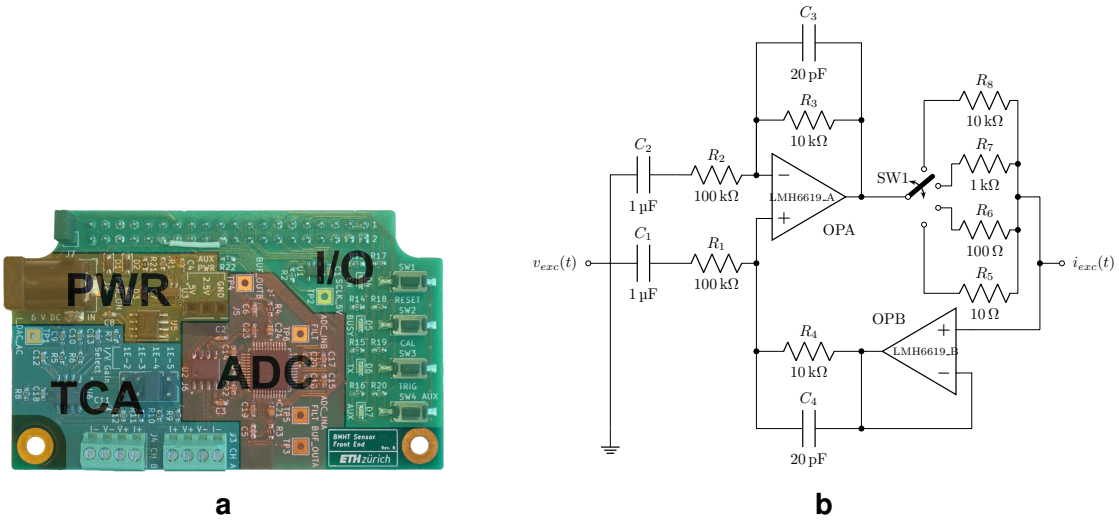

Figure S2: **Analog front end PCB and TCA schematic. a**, The analog front-end PCB with the power regulation, input/output, and TCA and ADC components delineated. **b**, The transconductance amplifier consists of a modified Howland current source using OPA with AC decoupling input capacitors C_1, C_2; selectable gain determined by R_1, R_2, jumper SW1, and R_5 through R_8; feedback buffer OPB; and noise filtering set by R_3, C_3, R_4, and C_4.

converted to a current signal $i_{exc}(t)$ and low-pass filtered to remove the undesired quantization noise. It is critical that the TCA provides accurate current output because $i_{exc}(t)$ itself is not measured. We designed the transconductance amplifier (TCA) shown in Fig. S2b for this purpose using a Howland current pump topology with a buffered feedback path to ensure consistent amplitude across the frequency range (*49*). Single pole RC circuits in the op-amp negative feedback paths were tuned with a SPICE model to balance quantization noise rejection with roll-off at the upper operating limit of 99.6 kHz. Jumper pins connected to SW1 allow the voltage-to-current gain G of the TCA to be adjusted between 10^{-2} A V^{-1} and 10^{-5} A V^{-1} to broaden the range of measurable impedances.

S1.4 Analog-to-Digital Converter

The core of the ADC block is the AD7724 (Analog Devices, Norwood, MA, USA) seventh-order $\Sigma\Delta$M integrated circuit shown as placed on our PCB in Fig. S2a. This high-performance

ADC digitizes the $v_{meas}(t)$ signal and provides an oversampled single-bit bitstream output that is received by the FPGA. The ADC is preceded by a low-pass RC filter with a 105 kHz cutoff frequency to provide antialiasing and further quantization noise removal. Because low-pass filtering is required for extracting the in-phase and quadrature signals $\hat{I}_i[k]$, $\hat{Q}_i[k]$, the digital reconstruction filter required for the ADC is instead combined with the low-pass filters at the end of the signal processing pipeline.

S1.5 Phase-Sensitive Demodulator

To reduce the digital circuit complexity, we implement digital mixers directly on the sigma-delta bitstream to avoid the use of costly hardware multipliers. Arithmetic and logic operations are commonly performed on $\Sigma\Delta$ bitstreams, including multiplication using the delta adder (*50, 51*). The mixers in our implementation operate on a 16-bit sinusoid reference signal and the single-bit sigma-delta bitstream $v_{meas}[k]$. This simple case reduces the mixers to just one multiplexer and a 2's complement negation, in a similar method as (*52*). Each sinusoid sample is passed through unchanged if a '1' symbol is encountered in the bitstream and negated if a '0' symbol is encountered. The resulting words are then filtered to reconstruct the modulated signal and extract the DC components shown in equations (9) and (10) of the main text. We used a cascaded integrator comb (CIC) filter architecture because of its low area requirements, which is important in this application because $2 \cdot N_f$ filters are required, despite the iCE40 FPGA family having relatively few logic resources. We used the Hogenauer pruning algorithm to set the integrator and comb register widths to further conserve logic elements (*53*). The third-order ($N = 3$, $M = 1$) CIC filter we designed has a very high decimation ratio of $R = 2^{18}$ to reduce the 6.375 MHz oversampled data stream to a manageable ca. 24 Hz output data rate. The block diagram of the CIC filter is shown in Fig. S3.

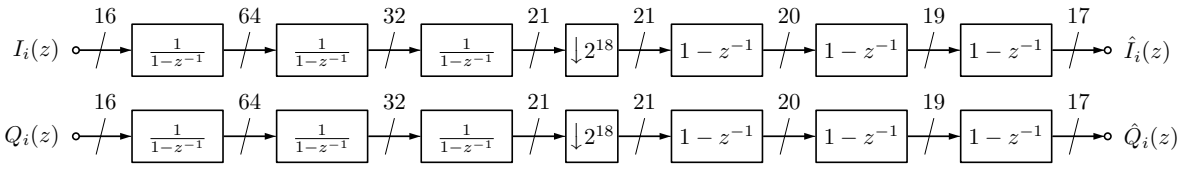

Figure S3: The architecture of the CIC decimation filter consists of a sign extension block, 3 discrete-time integrators, a decimator, and 3 feed-forward comb sections for the in-phase I and quadrature Q components of each frequency channel i.

S1.6 Communication and Client Software

The output communication block implements a first-in-first-out sample buffer and a finite state machine to generate frames according to the MIN protocol (*54*). A linear feedback shift register generates a CRC-32 checksum to ensure data parity. Finally, a UART sends the output frames over a serial port. A custom Python program running on the PC receives the data packets, applies calibration, and converts them to the desired interpretation (I/Q, magnitude/phase, RC or RL circuit, or converted to estimated strain using a computer model). Processed data are then saved to a file and optionally displayed in real-time plots.

S1.7 Digital Logic Implementation

We used the open-source IceStorm toolchain (*55*) for logic simulation, synthesis, routing, and FPGA programming. FPGA resource utilization for our system with $N_f = 4$ is listed in Table S1. All timing constraints were satisfied with the critical path having a maximum frequency in excess of 80 MHz.

S2 System Calibration Procedure

The system was calibrated using the LCR as a reference. The intent of calibration was to have reasonably accurate impedance values in real units, rather than to obtain perfect agreement with the LCR. The initial calibration was done to tune the compensation delay line length. The ideal

Table S1: Resource usage on the Lattice iCE40HX-8K low-cost FPGA.

Logic Type	**Utilization**	**%**
Logic element (LUT)	6982/7680	90%
RAM block	17/32	53%
I/O pin	35/256	13%
PLL block	1/2	50%

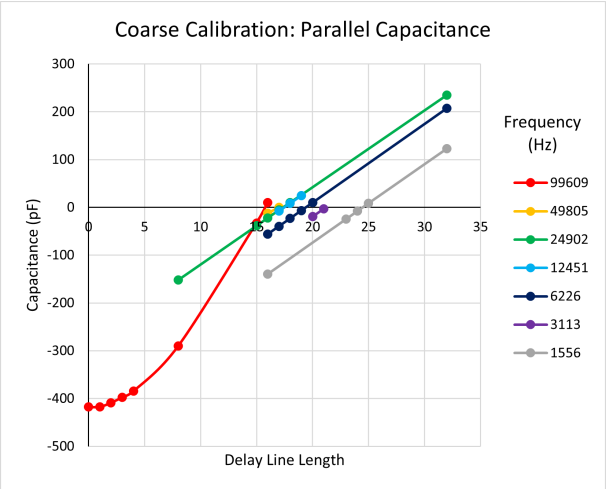

Figure S4: Delay line length versus indicated parallel capacitance, coloured by excitation frequency.

value of m_i is equal to the phase shift through the analog signal path at that frequency. Starting values were obtained from SPICE simulations, then fine tuned experimentally with a 10 kΩ resistive load. The ideal delay line length would result in a purely real impedance measurement (zero capacitance). Thus, m_i was tuned from the data collected in Fig. S4, choosing the value where the curve corresponding to each excitation frequency crosses through zero.

The next step of calibration was done using a series of 6 resistive loads (Table S2a) with reference values measured using the LCR meter. These measurements were used to construct a frequency-dependent linear calibration factor for the in-phase component, $\hat{I}_i[k]$, shown in Fig S9a. The quadrature component, $\hat{Q}_i[k]$, was tuned using a similar method with 12 RC-parallel loads (Table S2b), shown in Fig. S5b.

Table S2: **Nominal values for the calibration standards.** **a**, In-phase component (purely resistive loads). **b**, Quadrature component (RC-parallel loads).

a

Resistance
1.5 kΩ
2.2 kΩ
3.3 kΩ
4.7 kΩ
6.8 kΩ
10 kΩ

b

Resistance	Capacitance	Resistance	Capacitance
33 kΩ	1.0 pF	33 kΩ	47 pF
33 kΩ	2.2 pF	33 kΩ	68 pF
33 kΩ	4.7 pF	33 kΩ	100 pF
33 kΩ	6.8 pF	33 kΩ	220 pF
33 kΩ	10 pF	33 kΩ	470 pF
33 kΩ	22 pF	33 kΩ	680 pF

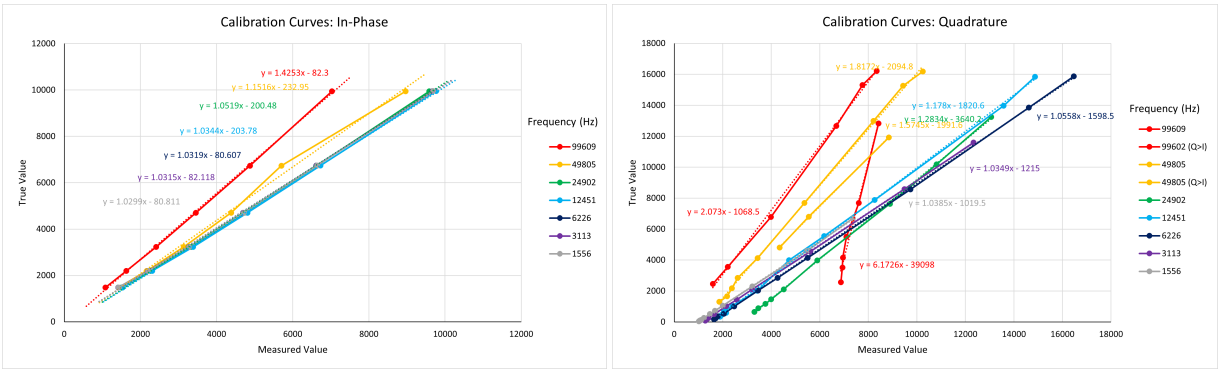

a **b**

Figure S5: **Calibration curves measured with the purely resistive and RC-parallel standards, coloured by excitation frequency.** **a**, In-phase. **b**, Quadrature.

Note that the highest frequency, 99.6 kHz (shown in red), is consistently lower for both in-phase and quadrature components than the reference value. This is due to the roll-off of the TCA filters at high frequency. During the quadrature calibration, a piecewise linear relationship was observed for high frequencies (99.6 kHz and 49.8 kHz), depending on whether the in-phase or quadrature component had higher magnitude (see Fig. S5b).

To verify that our calibration was sufficient for the types of sensors we fabricated, we measured the response of one sensor at a single frequency (10 kHz) and compared it to the LCR as strain was swept from 0%–40%–0% in a staircase pattern. The results are shown in Fig. S6 and

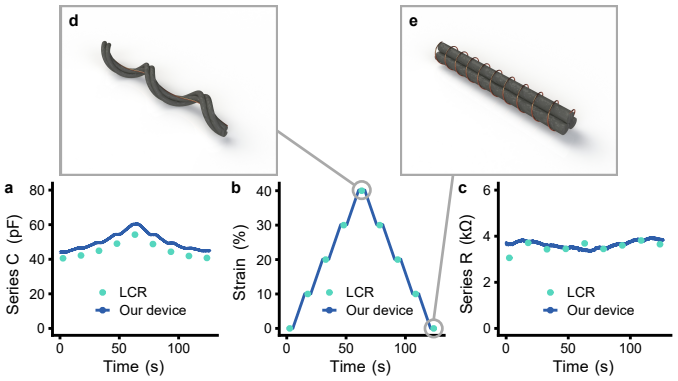

Figure S6: **Single sensor testing at 10 kHz.** **a**, The series capacitance of a single sensor segment at a single frequency during the staircase strain pattern, comparing our calibrated device to the LCR. **b**, The strain pattern produced by the UTM. **c**, The series resistance of the sensor agrees closely between the two readout methods and shows low piezoresistivity. **d**, A rendering of the sensor in strained, "flipped" state. **e**, A rendering of the sensor in unstrained state.

show close agreement to the LCR gold standard.

S3 Identifiability Analysis of the RC Ladder System

We seek to prove that the lumped approximation of the distributed transmission line sensor model is identifiable. In systems theory, the concept of *structural identifiability* means that it is theoretically possible to infer the true parameter values from input-output data (*56, Ch. 5.1.6*). Specifically, *global* structural identifiability means that a unique value can be estimated for each parameter, whereas *local* structural identifiability is a weaker concept and means that the parameter can be estimated to one of finitely many values (*57*). In the case of the sensor model, these parameters are the resistances R_i and capacitances C_i at each stage i along the chain, as shown in Fig. 3b of the main article. We operate here on the 3- or 4-segment lumped model rather than the distributed parameter system. An important caveat to identifiability analysis is that in order to guarantee identifiability, it assumes constant parameters and an infinite number of perfect measurements. Only limited information is gained about the type of input signal necessary to obtain accurate parameter estimations. Therefore, we do not claim that this analysis

is sufficient to prove completely that the distributed strain reconstruction is unique in practice, rather it is a piece of evidence to support our findings in the paper and claims from other articles.

First, we introduce the concept behind identifiability analysis. Consider a linear regression model with observations $y(t)$, regressors $x_i(t)$, and parameters θ_i.

$$y(t) = \theta_0 + x_1(t)\theta_1 + x_2(t)\theta_2 + \ldots + x_n(t)\theta_n + \epsilon$$

Assume we wish to find the parameters so that the linear model minimizes error ϵ in the least-squares sense. By concatenating observations and parameters into column vectors and stacking regressors into the matrix X, we obtain the familiar equation:

$$\vec{\theta} = \left(X^T X\right)^{-1} X^T \vec{y}. \tag{S1}$$

Equation (S1) is solvable if the number of linearly independent columns of X is greater than or equal to the number of regression parameters, i.e. $\mathrm{rank}(X) \geq n$. Conversely, the system is underdetermined if either there are fewer observations than parameters, or there are linearly dependent columns of X. This rank test concept can be generalized to dynamic systems in order to analyze structural identifiability. We introduce the general steps here and later provide a script that analyzes our systems of interest. Given a system T represented in the form of a vector of ordinary differential equations (ODEs):

$$T = \begin{cases} \dot{x}(t) = f(x(t), u(t), \theta) \\ y(t) = h(x(t), u(t), \theta). \end{cases} \tag{S2}$$

Where f and y are vector functions of the states x and input u, and θ is a vector of the unknown parameters, we can expose the unknown parameters as constant states. Assuming these parameters are slowly varying compared to $x(t)$, their derivatives are equal to zero. The augmented system with states $\tilde{x} = \begin{bmatrix} x(t) & \theta \end{bmatrix}^T$ is shown in equation (S3).

$$\tilde{T} = \begin{cases} \dot{\tilde{x}}(t) = \begin{bmatrix} f(x(t), u(t), \theta) & \vec{0}_{n_\theta} \end{bmatrix}^T = \tilde{f}(\tilde{x}(t), u(t)) \\ y(t) = \tilde{h}(\tilde{x}(t), u(t)) \end{cases} \tag{S3}$$

We must now introduce the Lie derivative, which is necessary to construct the observability-identifiability matrix for the system from equation (S2).

Definition 1 (Lie derivative (*58, Def. 1*))**.** The Lie derivative $L_{\tilde{f}}$ of the output function h with respect to $\tilde{x}$ along the vector field $\tilde{f}$ is:

$$L_{\tilde{f}} h\left(\tilde{x}(t), u(t)\right) = \frac{\partial \tilde{h}}{\partial \tilde{x}}\left(\tilde{x}(t), u(t)\right) \cdot \tilde{f}\left(\tilde{x}(t), u(t)\right).$$

Furthermore, the i^{th} Lie derivative can be computed recursively as:

$$L^i_{\tilde{f}} = \begin{cases} \tilde{h}\left(\tilde{x}(t), u(t)\right) & i = 0 \\ L_{\tilde{f}}\left(L^{i-1}_{\tilde{f}} \tilde{h}\left(\tilde{x}(t), u(t)\right)\right) & i \geq 1. \end{cases}$$

The observability-identifiability matrix $\mathcal{O}$ can then be formed by taking Lie derivatives up to order $n_{\tilde{x}} = n_x + n_\theta$:

$$\mathcal{O} = \frac{\partial}{\partial \tilde{x}} \begin{bmatrix} L^0_{\tilde{f}} h\left(\tilde{x}(t), u(t)\right) \\ L^1_{\tilde{f}} h\left(\tilde{x}(t), u(t)\right) \\ \vdots \\ L^{n_{\tilde{x}}-1}_{\tilde{f}} h\left(\tilde{x}(t), u(t)\right) \end{bmatrix}. \tag{S4}$$

The matrix from equation (S4) may be expressed in a similar form as X in equation (S1). The main result states that the parameters θ are locally identifiable if and only if $\operatorname{rank}\left(\mathcal{O}\right) = n_{\tilde{x}}$ (*59*). In the case that $\mathcal{O}$ is rank-deficient, we may have to consider the form of the input $u(t)$ (*60*). By using the extended Lie derivative (*61, Eq. 3*) and including terms for various time derivatives of $u(t)$, it is also possible to analyze the structural identifiability of $\tilde{T}$ under non-constant input.

For our specific system, identifiability analysis begins from the lumped approximation of the distributed impedance model (equation (2) in the main text). Taking the inverse to obtain

the admittance transfer function then converting to a state-space model with capacitor voltages as states, we obtain equation (S5).

$$\overbrace{\frac{d}{dt}\begin{bmatrix} v_1(t) \\ v_2(t) \\ v_3(t) \\ v_4(t) \end{bmatrix}}^{\dot{\vec{x}}} = \overbrace{\begin{bmatrix} -\frac{1}{R_1C_1} & \frac{1}{R_1C_1} & 0 & 0 \\ \frac{1}{R_1C_2} & -\frac{1}{C_2}\left(\frac{1}{R_1}+\frac{1}{R_2}\right) & \frac{1}{R_2C_2} & 0 \\ 0 & \frac{1}{R_2C_3} & -\frac{1}{C_3}\left(\frac{1}{R_2}+\frac{1}{R_3}\right) & \frac{1}{R_3C_3} \\ 0 & 0 & \frac{1}{R_3C_4} & -\frac{1}{C_4}\left(\frac{1}{R_3}+\frac{1}{R_4}\right) \end{bmatrix}}^{A} \overbrace{\begin{bmatrix} v_1(t) \\ v_2(t) \\ v_3(t) \\ v_4(t) \end{bmatrix}}^{\vec{x}} + \overbrace{\begin{bmatrix} 0 \\ 0 \\ 0 \\ \frac{1}{R_4C_4} \end{bmatrix}}^{B} v_{meas}(t)$$

$$i_{exc}(t) = \underbrace{\begin{bmatrix} 0 & 0 & 0 & -\frac{1}{R_4} \end{bmatrix}}_{C} \begin{bmatrix} v_1(t) \\ v_2(t) \\ v_3(t) \\ v_4(t) \end{bmatrix} + \underbrace{\frac{1}{R_4}}_{D} v_{meas}(t) \tag{S5}$$

With the ODEs from equation (S5), we may proceed with the identifiability analysis. We perform this analysis using the computer algebra software Maple 2021 (MapleSoft, Waterloo, ON, CA) with the scripts available in our repository[1] and the Appendix. These scripts include the following:

1. `RC3Identifiability.mw` (Appendix A.1) Local structural identifiability analysis using a custom script implementing the algorithm outlined above, for the case of the lumped RC ladder system with 3 stages (modelling the sensor layout used in Section 2 *Joint Angle Monitoring* of the main article).

2. `RC4Identifiability.mw` (Appendix A.2) Local and global structural identifiability analysis computed with the SIAN tool (*57*) for the case of the lumped RC ladder system with 4 stages (modelling the sensor layout used in Section 2 *Localized Strain Reconstruction* of the main article).

We found in 1. that the system is at least locally structurally identifiable if the input signal derivatives up to order 3 were included. This indicates that the lumped system parameters may

[1] `https://gitlab.ethz.ch/BMHT/publications/distributed-sensing-along-fibres`

be estimated to a finite number of values if a sufficiently exciting input signal is provided, such as the sum of sines used in our readout electronics. Because of computation time, we employed the open-source software SIAN to analyze the 4-segment system in 2., which also provides information about more rigorous global identifiability. This computational tool includes some approximations to speed computation, for which there is a probability bound specified by the user to trade off computation time and accuracy. The results from the computation indicate that all 8 parameters of the system are globally structurally identifiable with probability bound 0.999.

S4 Effect of Bending on Sensor Response

The sensors were characterized on a UTM using unidirectional strain. In the garment, the sensors are strained while undergoing bending around the joint. To better investigate the effect of simultaneous bending on the sensor response, the sensors were tested on a jig with varying radii of 12 cm to 4 cm, in order to resemble what they may be exposed to on the garment. The response $\frac{C(\varepsilon)-C(0)}{C(0)}$ was calculated for three strain levels of approximately 20%, 40%, and 60%. The tests were run for three sensor samples and the data compared to the response during strain without bending (infinite radius). From the results shown in Fig. S7, no strong relationship between radius and response is observed. There is a slight increase in response when bent at small radii, but the variance between samples is generally greater than the variance because of bending radius.

S5 Cyclic Durability Tests

A durability test was performed to examine the effect of wear that the garment would experience during normal use, under controlled conditions. Particularly, it was desired to determine if any change in sensitivity of the highly-sensitive and insensitive regions would occur because

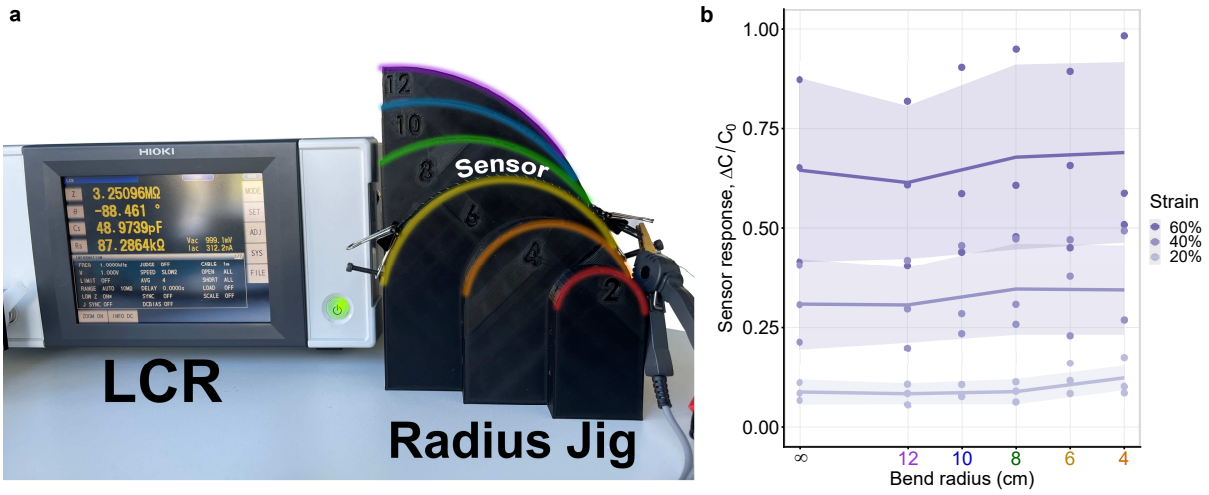

Figure S7: **Simultaneous strain and bending test**. **a**, The experimental test set-up, where the sensor response is measured at different strain levels while being bent around varying radii. **b**, Response of the sensors versus bend radius at three strain levels, where the solid line is the average response and the shaded regions indicate the 90% confidence interval between 3 samples.

of wear and friction. A sensing fibre sample with one 8 cm highly-sensitive region and one 8 cm insensitive region was attached to a coupon of fabric in the same way as the garment described in Section 4 *Fibre Sensor and Prototype Garment Fabrication* of the main text. The two regions had respectively 8 mm and 3.5 mm pitch to exactly resemble those used in the garment. The test coupon was mounted in the UTM (Fig. S8e) and the custom electronics were used to record the impedance signals at the four frequencies 12.5 kHz, 25 kHz, 50 kHz, and 100 kHz. A triangular strain profile from 0% to 25% was applied to measure the pre-cyclic testing response (Fig. S8a) and the gauge factor was calculated using the LCR gold standard measurement device, separately for each sensitivity region, and also for the series connection of both (entire sensor line) (Fig. S8d). Following this, the sample was exposed to 1 000 cycles of straining from 2.5% to 22.5% with a 0.5 Hz sinusoidal profile. Fig. S8b shows the evolution of the impedance signals at each of the excitation frequencies over the 1 000 cycles, recorded with the custom electronics. After this cyclic testing, the response and gauge factor was again

measured in the same fashion (Fig. S8c, S8f). We observed very little drift in the signal across the cyclic tests, and nearly identical gauge factors for each region. These results indicate that the helical sensor configuration is robust against cyclic wear both in the high-sensitivity and low-sensitivity configurations. There was an small plastic deformation that occurred primarily in the textile backing during the first few extensions. This may been seen in Fig. S8 where the signal is close to zero for strain below 5% and can be avoided with a mechanical pre-conditioning step prior to manufacture. The pitch of each twist was also measured with calipers before and after the cyclic testing with the results listed in Table S3. The difference in means between before and after for both regions were found to be insignificant ($p = 0.84$ and $p = 0.56$, respectively).

S6 Validation Experiment Set-Up

The validation experiment discussed in Section 2 *Localized Strain Reconstruction* of the main text is shown in Fig. S9b. The system includes the UTM tensile tester interfaced with the custom made independent strain fixture. The readout system connects to the strain sensitive fibre, is synchronized to the UTM, and is logged by a PC. The LCR device is intermittently connected to provide a validation reference.

S7 Full Strain Reconstruction Results

Table S4 shows the full accuracy (RMSE) and correlation (R^2) scores for the strain reconstruction experiment.

S8 Joint Angle Monitoring Experiment Set-Up

Fig. S10 demonstrates the garment as worn during the joint angle monitoring experiment. The path of the strain sensitive fibre along the left arm may be seen in a selection of poses done during the data collection. The upper-body OMC marker positions are also shown.

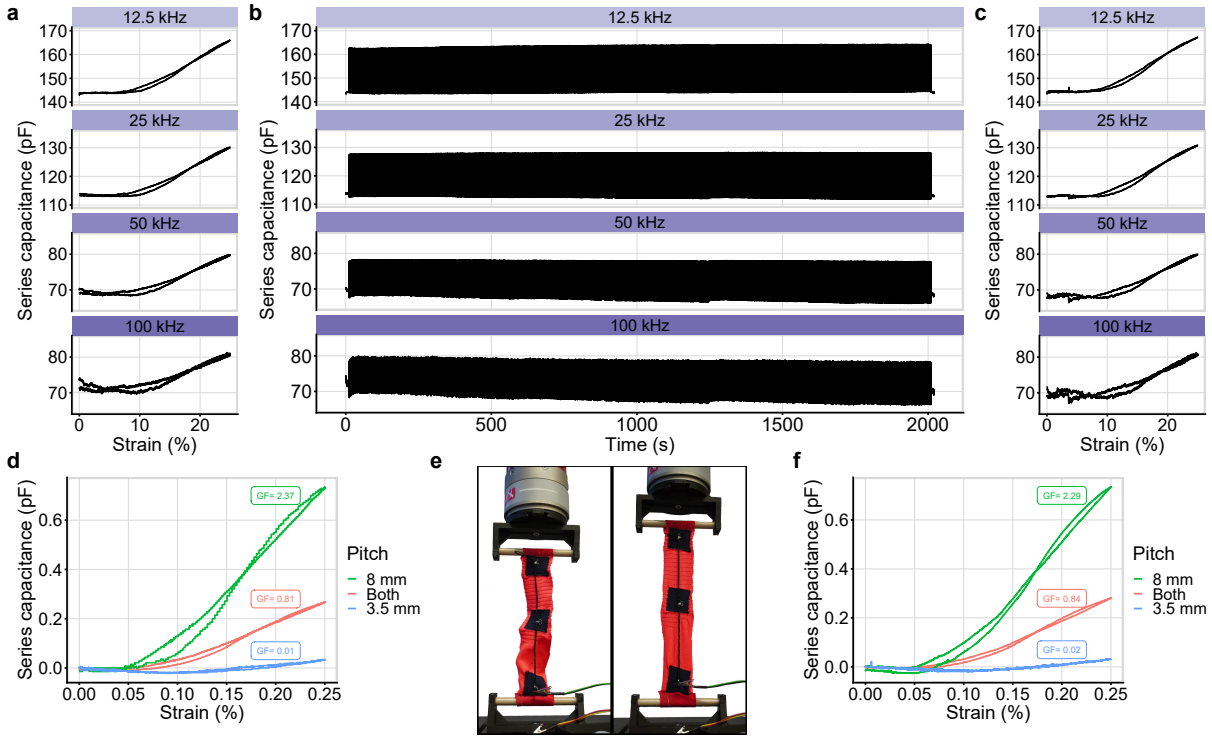

Figure S8: **Cyclic durability test.** **a**, Sensor series capacitance response to a triangular strain pattern at the four excitation frequencies prior to the cyclic durability test. **b**, Sensor series capacitance at each frequency during 1000 cycles of 20% strain. **c**, Sensor series capacitance response to a triangular strain pattern at the four excitation frequencies after the cyclic durability test. **d**, Gauge factor quantified for the highly-sensitive region (green), insensitive region (blue), and entire sensor (red), prior to the cyclic durability test. **e**, Photograph of the test set-up. **f**, Gauge factor quantified after the cyclic durability test.

Table S3: Measurements of pitch for the sensitive and insensitive regions of the fibre before and after 1 000 cycles of straining to 22.5%.

Twist	**Highly-Sensitive Region (mm)**			**Insensitive Region (mm)**		
	Nominal	**Before**	**After**	**Nominal**	**Before**	**After**
1	8.00	7.57	7.00	3.50	2.72	3.39
2	8.00	7.66	7.44	3.50	1.94	3.47
3	8.00	7.94	7.80	3.50	2.32	2.68
4	8.00	8.16	8.70	3.50	3.52	2.55
5	8.00	8.84	7.75	3.50	3.64	3.06
6	8.00	7.90	7.18	3.50	2.52	4.31
7	8.00	7.65	7.91	3.50	3.15	2.47
8	8.00	7.70	7.57	3.50	3.14	2.74
9	8.00	7.23	8.87	3.50	3.30	3.36
10	8.00	7.43	7.36	3.50	3.18	3.36
11				3.50	3.50	3.26
12				3.50	3.04	3.83
13				3.50	3.74	3.06
14				3.50	3.19	3.50
15				3.50	3.60	3.39
16				3.50	3.03	3.67
17				3.50	4.00	3.12
18				3.50	3.68	3.95
19				3.50	3.84	3.60
20				3.50	3.81	4.05
	Mean:	7.81	7.76	**Mean:**	2.94	3.34
	SD:	0.45	0.61	**SD:**	0.55	0.50

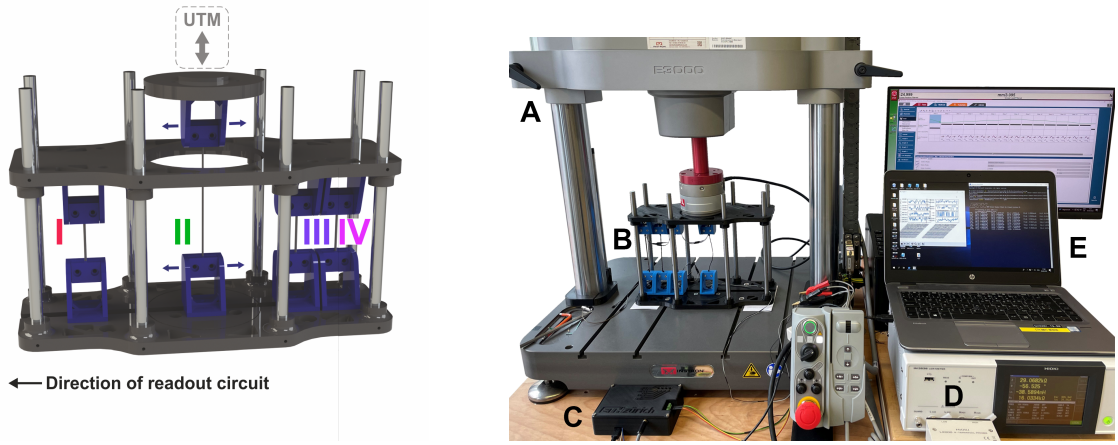

Figure S9: **Design of the independent strain fixture and associated validation experiment set-up. a**, 3D model rendering of the fixture and the positioning of sensor segments I–IV within it. **b**, Data collection set-up, including: **A**, UTM; **B**, independent strain fixture; **C**, readout electronics; **D**, LCR meter; **E**, PC running client software.

Figure S10: Side and rear view of the prototype garment, sensing fibre path, and OMC marker placement for some sample poses during the joint angle monitoring data collection.

Table S4: RMSE and R^2 scores of MLP strain reconstruction algorithm performance across the training, test, and validation sets, separated by sensor segment I–IV, number of sensors being strained simultaneously 'Single'/'Double', and overall performance 'All'.

	Train		**Validation**		**Test**		**Avg.**	
Segment	RMSE	R^2	RMSE	R^2	RMSE	R^2	RMSE	R^2
I	0.0074	0.9953	0.0100	0.9916	0.0112	0.9895	0.0086	0.9937
II	0.0109	0.9924	0.0116	0.9913	0.0129	0.9892	0.0114	0.9917
III	0.0066	0.9972	0.0081	0.9957	0.0093	0.9945	0.0074	0.9965
IV	0.0077	0.9950	0.0079	0.9947	0.0083	0.9942	0.0079	0.9948
Single	0.0059	0.9965	0.0082	0.9936	0.0101	0.9903	0.0072	0.9949
Double	0.0104	0.9929	0.0107	0.9924	0.0108	0.9924	0.0105	0.9928
Avg.	0.0082	0.9950	0.0094	0.9933	0.0104	0.9918	0.0088	0.9942

S9 Full Joint Angle Regression Results

The tables below provide full fold-by-fold coefficients of determination (R^2, Table S5a) and root mean squared error (RMSE, Table S5b) for the joint angle regression problem using the MLP model from main text Section 2 *Joint Angle Monitoring*. Fold 10 was used to obtain the results reported in the main text. Fig. S11 shows the predicted versus reference joint angles for each cross-validation fold.

Table S5: **Full fold-by-fold results for joint angle reconstruction.** **a**, R^2 goodness of fit. **b**, Root mean squared error.

a

	Train				Validation				Test				
Fold	Shoulder	Elbow	Wrist	Avg.	Shoulder	Elbow	Wrist	Avg.	Shoulder	Elbow	Wrist	Avg.	**Avg.**
1	0.967	0.990	0.880	0.946	0.966	0.990	0.878	0.945	0.909	0.988	0.653	0.850	0.913
2	0.969	0.989	0.878	0.945	0.968	0.990	0.874	0.944	0.946	0.976	0.719	0.880	0.923
3	0.963	0.989	0.884	0.945	0.963	0.989	0.887	0.946	0.963	0.989	0.450	0.801	0.898
4	0.970	0.987	0.873	0.943	0.970	0.986	0.872	0.943	0.967	0.988	0.818	0.924	0.937
5	0.968	0.989	0.876	0.944	0.966	0.989	0.879	0.945	0.975	0.988	0.809	0.924	0.938
6	0.964	0.987	0.870	0.940	0.963	0.988	0.874	0.942	0.965	0.989	0.877	0.944	0.942
7	0.963	0.990	0.873	0.942	0.963	0.991	0.875	0.943	0.959	0.989	0.871	0.940	0.942
8	0.967	0.987	0.880	0.945	0.967	0.987	0.879	0.944	0.970	0.986	0.848	0.935	0.941
9	0.963	0.988	0.872	0.941	0.963	0.989	0.872	0.941	0.956	0.984	0.840	0.927	0.936
10	0.966	0.989	0.876	0.944	0.965	0.989	0.881	0.945	0.949	0.966	0.831	0.915	0.935
Avg.	0.966	0.989	0.876	0.944	0.965	0.989	0.877	0.944	0.956	0.984	0.772	0.904	0.930

b

	Train				Validation				Test				
Fold	Shoulder	Elbow	Wrist	Avg.	Shoulder	Elbow	Wrist	Avg.	Shoulder	Elbow	Wrist	Avg.	**Avg.**
1	4.0°	3.4°	5.4°	4.2°	4.0°	3.4°	5.3°	4.2°	5.7°	3.8°	11.9°	7.1°	5.2°
2	3.8°	3.5°	5.6°	4.3°	3.9°	3.5°	5.7°	4.4°	5.1°	4.9°	7.7°	5.9°	4.9°
3	4.2°	3.6°	5.5°	4.4°	4.1°	3.6°	5.5°	4.4°	4.2°	3.3°	10.4°	6.0°	4.9°
4	3.8°	3.9°	5.8°	4.5°	3.8°	3.9°	5.7°	4.5°	3.7°	3.8°	6.0°	4.5°	4.5°
5	3.9°	3.6°	5.6°	4.4°	3.9°	3.6°	5.6°	4.4°	3.6°	3.8°	7.2°	4.9°	4.5°
6	4.1°	3.8°	5.8°	4.6°	4.1°	3.8°	5.7°	4.5°	4.2°	3.6°	5.4°	4.4°	4.5°
7	4.2°	3.3°	5.7°	4.4°	4.2°	3.3°	5.7°	4.4°	4.3°	3.6°	5.4°	4.4°	4.4°
8	3.9°	3.8°	5.5°	4.4°	4.0°	3.9°	5.5°	4.5°	3.8°	4.1°	6.5°	4.8°	4.6°
9	4.2°	3.7°	5.7°	4.5°	4.2°	3.6°	5.7°	4.5°	4.5°	4.2°	6.3°	5.0°	4.7°
10	4.0°	3.5°	5.6°	4.4°	4.0°	3.5°	5.6°	4.4°	4.9°	6.5°	6.1°	5.8°	4.9°
Avg.	4.0°	3.6°	5.6°	4.4°	4.0°	3.6°	5.6°	4.4°	4.4°	4.1°	7.3°	5.3°	4.7°

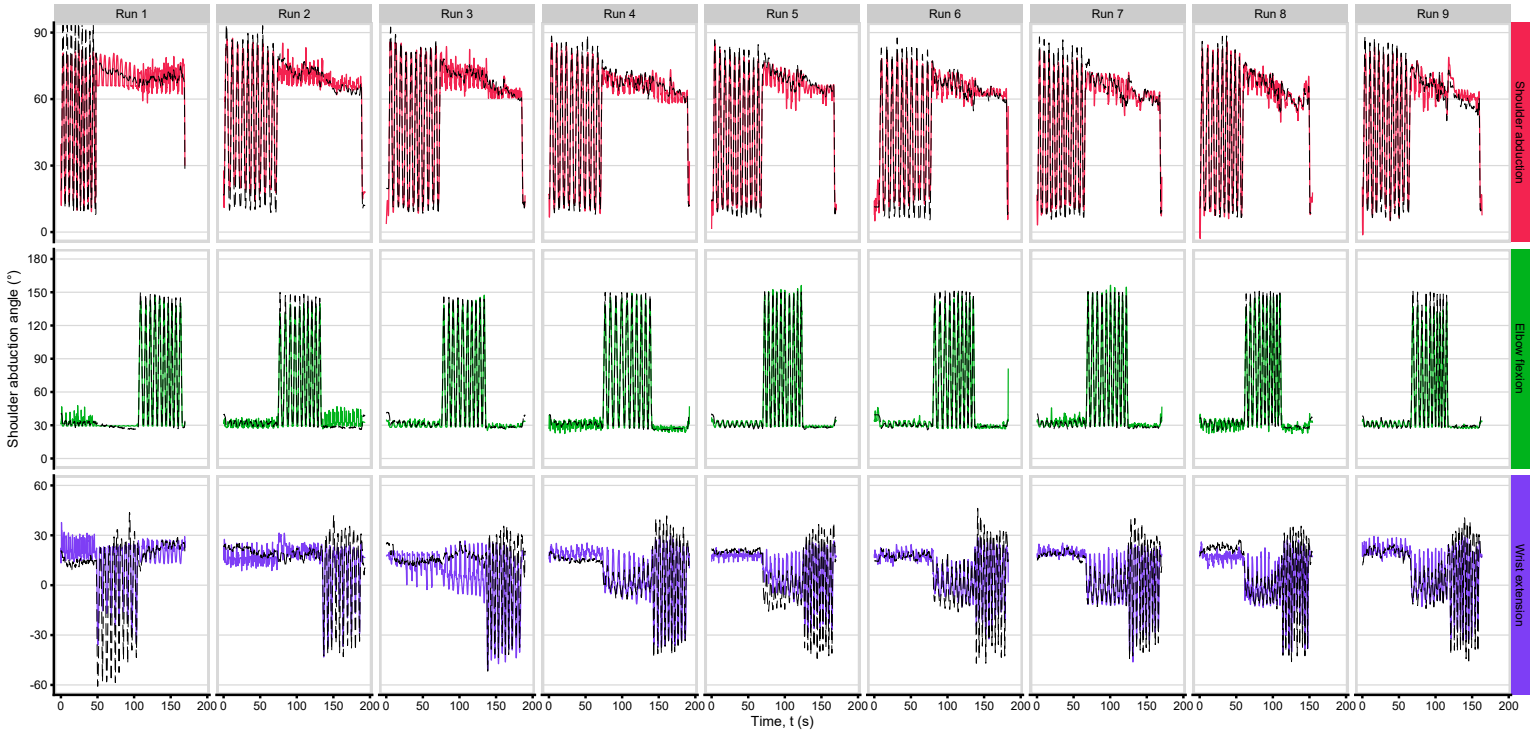

Figure S11: Folds 1–9 of joint angle reconstruction cross-validation on the test dataset.

A Appendices

A.1 Identifiability Analysis of 3-Segement RC Ladder

Identifiability Analysis of 3-Segement RC Ladder

This script corresponds to the analysis performed in 1. in the Supplementary Materials Section S3.

Define the system of differential equations, output equation, parameter vector, and a vector of derivatives of the input.

> $states := Vector[column](3, symbol = x);$

$$f := (x, \theta, u) \rightarrow \begin{bmatrix} -\frac{1}{\theta[1]\cdot\theta[4]}\cdot x[1] + \frac{1}{\theta[1]\cdot\theta[4]}\cdot x[2] \\ \frac{1}{\theta[1]\cdot\theta[5]}\cdot x[1] - \frac{1}{\theta[5]}\cdot\left(\frac{1}{\theta[1]} + \frac{1}{\theta[2]}\right)\cdot x[2] + \frac{1}{\theta[2]\cdot\theta[5]}\cdot x[3] \\ \frac{1}{\theta[2]\cdot\theta[6]}\cdot x[2] - \frac{1}{\theta[6]}\cdot\left(\frac{1}{\theta[2]} + \frac{1}{\theta[3]}\right)\cdot x[3] + \frac{1}{\theta[3]\cdot\theta[6]}\cdot u \end{bmatrix};$$

$$h := (x, \theta, u) \rightarrow -\frac{1}{\theta[3]}\cdot x[3] + \frac{1}{\theta[3]}\cdot u;$$

$param := Vector[column](6, symbol = \theta);$

$udot := ArrayTools[Concatenate](1, Vector[column](4, symbol = u), Vector[column](5))$

$$states := \begin{bmatrix} x_1 \\ x_2 \\ x_3 \end{bmatrix}$$

$$f := (x, \theta, u) \mapsto rtable\left(1..3, \left[-\frac{x_1}{\theta_1\cdot\theta_4} + \frac{x_2}{\theta_1\cdot\theta_4}, \frac{x_1}{\theta_1\cdot\theta_5} - \frac{\left(\frac{1}{\theta_1} + \frac{1}{\theta_2}\right)\cdot x_2}{\theta_5} + \frac{x_3}{\theta_2\cdot\theta_5}, \frac{x_2}{\theta_2\cdot\theta_6} - \frac{\left(\frac{1}{\theta_2} + \frac{1}{\theta_3}\right)\cdot x_3}{\theta_6} + \frac{u}{\theta_3\cdot\theta_6}\right], subtype = Vector_{column}\right)$$

$$h := (x, \theta, u) \mapsto -\frac{x_3}{\theta_3} + \frac{u}{\theta_3}$$

$$param := \begin{bmatrix} \theta_1 \\ \theta_2 \\ \theta_3 \\ \theta_4 \\ \theta_5 \\ \theta_6 \end{bmatrix}$$

$$udot := \begin{bmatrix} u_1 \\ u_2 \\ u_3 \\ u_4 \\ 0 \\ 0 \\ 0 \\ 0 \\ 0 \end{bmatrix} \quad \textbf{(1)}$$

Construct the augmented system, where parameters are exposed as additional states with their derivative equal to zero.

```
> with(ArrayTools):
  x_aug := Concatenate(1, states, param);
  f_aug := (x, u)→Concatenate(1, f(x[1..3], param, u), Vector[column](6));
  h_aug := (x, u)→h(x[1..3], param, u)
```

$$x\_aug := \begin{bmatrix} x_1 \\ x_2 \\ x_3 \\ \theta_1 \\ \theta_2 \\ \theta_3 \\ \theta_4 \\ \theta_5 \\ \theta_6 \end{bmatrix}$$

$$f\_aug := (x, u) \mapsto Concatenate\left(1, f\left(x_{1..3}, param, u\right), Vector_{column}(6)\right)$$

$$h\_aug := (x, u) \mapsto h\left(x_{1..3}, param, u\right) \quad \textbf{(2)}$$

Define the Lie derivative and the function for the recursive (ordinary) Lie derivative.

```
> lie_derivative := (h, x, f) -> VectorCalculus[Jacobian](h, convert(x, list)) . f;
  lie_derivative_n := proc(n :: nonnegint, h, x, u) :
    if n = 0 then
      return h :
    else
      return lie_derivative_n(n - 1, lie_derivative(h, x, u), x, u) :
    end if;
  end proc:
```

$$lie\_derivative := (h, x, f) \to Typesetting{:-}delayDotProduct\left(VectorCalculus_{Jacobian}(h, convert(x, list)), f\right) \quad \textbf{(3)}$$

Define the extended Lie derivative function following Ref. [59] from the SI.

```
> extended_lie_derivative_n := proc(n :: nonnegint, h, f, x, u) :
    if n = 0 then
      return h :
    else
      return extended_lie_derivative_n(n - 1, lie_derivative(h, x, f), f, x, u)
        + add(extended_lie_derivative_n(n - 1, lie_derivative(h, u[j], convert([u[j + 1]],
        Vector)), f, x, u), j = 1 ..4) :
    end if;
  end proc:
```

Warning, (in extended_lie_derivative_n) `j` is implicitly declared local

Build the observability-identifiability matrix.

```
> L := map(x -> extended_lie_derivative_n(x, [h_aug(x_aug, udot[1])], f_aug(x_aug, udot[1]),
       x_aug, udot)[1], Vector[column](9, i -> i - 1)) :
  O := VectorCalculus[Jacobian](L, convert(x_aug, list)) :
```

```
> LinearAlgebra[RowDimension](O)
```

$$9 \quad \textbf{(4)}$$

Compute the rank.

```
> LinearAlgebra[Rank](O)
```

$$9 \quad \textbf{(5)}$$

A.2 Identifiability Analysis of 4-Segement RC Ladder using SIAN

Identifiability Analysis of 4-Segment RC Ladder using SIAN

This script corresponds to the analysis performed in 2. in the Supplementary Materials Section S3.

Load SIAN (ref. [] from the Supplementary Materials).

```
> read "T:/SIAN/IdentifiabilityODE.mpl" :
```

sigma :=

$$
\begin{aligned}
&diff\left(x_1(t), t\right) = -\frac{1}{R_1 \cdot C_1} \cdot x_1(t) + \frac{1}{R_1 \cdot C_1} \cdot x_2(t),\\
&diff\left(x_2(t), t\right) = \frac{1}{R_1 \cdot C_2} \cdot x_1(t) - \frac{1}{C_2} \cdot \left(\frac{1}{R_1} + \frac{1}{R_2}\right) \cdot x_2(t) + \frac{1}{R_2 \cdot C_2} \cdot x_3(t),\\
&diff\left(x_3(t), t\right) = \frac{1}{R_2 \cdot C_3} \cdot x_2(t) - \frac{1}{C_3} \cdot \left(\frac{1}{R_2} + \frac{1}{R_3}\right) \cdot x_3(t) + \frac{1}{R_3 \cdot C_3} \cdot x_4(t),\\
&diff\left(x_4(t), t\right) = \frac{1}{R_3 \cdot C_4} \cdot x_3(t) - \frac{1}{C_4} \cdot \left(\frac{1}{R_3} + \frac{1}{R_4}\right) \cdot x_4(t) + \frac{1}{R_4 C_4} \cdot u(t),\\
&y(t) = -\frac{1}{R_4} \cdot x_4(t) + \frac{1}{R_4} \cdot u(t)
\end{aligned}
$$

```
Warning, (in IdentifiabilityODE) `poly_system` is implicitly
declared local |T:/SIAN/IdentifiabilityODE.mpl:2|
```

$$
\sigma := \left[\frac{d}{dt} x_1(t) = -\frac{x_1(t)}{R_1 C_1} + \frac{x_2(t)}{R_1 C_1}, \frac{d}{dt} x_2(t) = \frac{x_1(t)}{R_1 C_2} - \frac{\left(\frac{1}{R_1} + \frac{1}{R_2}\right) x_2(t)}{C_2} + \frac{x_3(t)}{R_2 C_2}, \frac{d}{dt} \right. \tag{1}
$$

$$
x_3(t) = \frac{x_2(t)}{R_2 C_3} - \frac{\left(\frac{1}{R_2} + \frac{1}{R_3}\right) x_3(t)}{C_3} + \frac{x_4(t)}{R_3 C_3}, \frac{d}{dt} x_4(t) = \frac{x_3(t)}{R_3 C_4} - \frac{\left(\frac{1}{R_3} + \frac{1}{R_4}\right) x_4(t)}{C_4}
$$

$$
\left. + \frac{u(t)}{R_4 C_4}, y(t) = -\frac{x_4(t)}{R_4} + \frac{u(t)}{R_4} \right]
$$

Perfom the analysis.

```
> IdentifiabilityODE(sigma, GetParameters(sigma), p = 0.999, infolevel = 2)

======================================================
0. Extracting states, inputs, outputs, and parameters from the
system
======================================================

=== Input info ===
State variables:          [x__1(t), x__2(t), x__3(t), x__4(t)]
```

```
Output variables:          [y(t)]
Input variables:           [u(t)]
Parameters in equations:   [C__1, C__2, C__3, C__4, R__1, R__2,
R__3, R__4]
===================


=====================================================
1. Constructing the maximal polynomial system
=====================================================

=====================================================
2. Truncating the polynomial system based on the Jacobian condition
=====================================================
Bound D_1 for testing the rank of the Jacobian probabilistically:
2408640000
Orders of prolongations of the outputs (beta) =  [13]
Orders of prolongations of the state variables (alpha) =  [10, 11,
12, 13]

=====================================================
3. Assessing local identifiability
=====================================================
Locally identifiable paramters:  [C__1, C__2, C__3, C__4, R__1,
R__2, R__3, R__4, x__1(0), x__2(0), x__3(0), x__4(0)]
Nonidentifiable parameter:  []

=====================================================
4. Randomizing the truncated system
=====================================================
Bound D_2 for assessing global identifiability:
17903573870000000000000000000000000
Random sample for the outputs and inputs is generated from  [C__1 =
1444961928005745719878993934560189054, C__2 =
945782520343874752725014146712799 78, C__3 =
204039316514760587353636419666237 42, C__4 =
159990195552613830032884526592025815, R__1 =
551502947493421371125118141132554 22, R__2 =
147408281933588652098259998059508103, R__3 =
822666961423379687145157681448426 04, R__4 =
135069511684012613289060082390337356, x__1_0 =
158264958354780925939464563956985268, x__2_0 =
503131995756158227219893204471378 2, x__3_0 =
789961333829451969766689410481103 18, x__4_0 =
155736813300766026337448996445453158]
The polynomial system widehat{E^t} contains  55 equations in  54
variables

=====================================================
Applying Weighted Ordering
=====================================================
Variable ordering to be used for Groebner basis computation
[x__4_12, x__4_11, x__3_11, x__4_10, x__3_10, x__2_10, x__4_9,
x__3_9, x__2_9, x__1_9, x__4_8, x__3_8, x__2_8, x__1_8, x__4_7,
x__3_7, x__2_7, x__1_7, x__4_6, x__3_6, x__2_6, x__1_6, x__4_5,
x__3_5, x__2_5, x__1_5, x__4_4, x__3_4, x__2_4, x__1_4, x__4_3,
x__3_3, x__2_3, x__1_3, x__4_2, x__3_2, x__2_2, x__1_2, x__4_1,
```

```
x__3_1, x__2_1, x__1_1, x__4_0, x__3_0, x__2_0, x__1_0, z_aux,
w_aux, C__1, C__2, C__3, C__4, R__1, R__2, R__3, R__4]
Weight assignment: [x__3_0 = x__3_0^2, x__1_1 = x__1_1^4, z_aux =
z_aux^3, x__2_7 = x__2_7^3, x__2_8 = x__2_8^3, x__2_9 = x__2_9^3,
x__1_0 = x__1_0^4, x__2_1 = x__2_1^3, x__2_6 = x__2_6^3, x__3_1 =
x__3_1^2, x__3_5 = x__3_5^2, x__3_2 = x__3_2^2, x__2_2 = x__2_2^3,
x__3_4 = x__3_4^2, x__3_6 = x__3_6^2, x__2_4 = x__2_4^3, x__3_3 =
x__3_3^2, x__4_6 = x__4_6, x__2_5 = x__2_5^3, x__4_1 = x__4_1,
x__4_10 = x__4_10, x__1_6 = x__1_6^4, x__4_2 = x__4_2, x__1_8 =
x__1_8^4, x__2_0 = x__2_0^3, x__4_12 = x__4_12, x__1_9 = x__1_9^4,
x__4_4 = x__4_4, x__3_7 = x__3_7^2, x__1_2 = x__1_2^4, x__1_5 =
x__1_5^4, x__4_3 = x__4_3, x__1_7 = x__1_7^4, x__4_11 = x__4_11,
x__4_9 = x__4_9, x__4_8 = x__4_8, x__2_10 = x__2_10^3, x__3_11 =
x__3_11^2, x__4_5 = x__4_5, x__3_9 = x__3_9^2, x__4_7 = x__4_7,
x__1_4 = x__1_4^4, x__3_10 = x__3_10^2, x__2_3 = x__2_3^3, x__3_8 =
x__3_8^2, x__1_3 = x__1_3^4, x__4_0 = x__4_0]

=======================================================
5. Assessing global identifiability
=======================================================
The number of solutions for C__1 is 1
The number of solutions for C__2 is 1
The number of solutions for C__3 is 1
The number of solutions for C__4 is 1
The number of solutions for R__1 is 1
The number of solutions for R__2 is 1
The number of solutions for R__3 is 1
The number of solutions for R__4 is 1
The number of solutions for x__1_0 is 1
The number of solutions for x__2_0 is 1
The number of solutions for x__3_0 is 1
The number of solutions for x__4_0 is 1

=== Summary ===
Globally identifiable parameters:                  [C__1, C__2,
C__3, C__4, R__1, R__2, R__3, R__4, x__1(0), x__2(0), x__3(0), x__4
(0)]
Locally but not globally identifiable parameters:  []
Not identifiable parameters:                       []
===============


=======================================================
WARNING: The result of solution counting is guaranteed with high
probability, however it NOT the same probability 'p' as provided in
the input.
=======================================================
```

output **(2)**

```
>
```

REFERENCES AND NOTES

1. D. Kim, J. Kwon, S. Han, Y. L. Park, S. Jo, Deep full-body motion network for a soft wearable motion sensing suit. *IEEE/ASME Trans. Mechatron.* **24**, 56–66 (2019).
2. Z. He, G. Zhou, J. H. Byun, S. K. Lee, M. K. Um, B. Park, T. Kim, S. B. Lee, T. W. Chou, Highly stretchable multi-walled carbon nanotube/thermoplastic polyurethane composite fibers for ultrasensitive, wearable strain sensors. *Nanoscale* **11**, 5884–5890 (2019).
3. F. Yin, X. Li, H. Peng, F. Li, K. Yang, W. Yuan, A highly sensitive, multifunctional, and wearable mechanical sensor based on RGO/synergetic fiber bundles for monitoring human actions and physiological signals*, Sens. Actuators B Chem.* **285**, 179–185 (2019).
4. R. Madhavan, Epidermis-like high performance wearable strain sensor for full-range monitoring of the human activities *Macromol. Mater. Eng* . **307**, 2200034 (2022).
5. L. Zhu, Y. Wang, D. Mei, L. Zhang, C. Mu, S. Wang, S. Dai, Z. Chen, Large-area hand-covering elastomeric electronic skin sensor with distributed multifunctional sensing capability *Adv. Intell. Syst.* **4**, 2100118 (2022).
6. A. Alian, G. Mylonas, J. Avery, Soft Continuum Actuator Tip Position and Contact Force Prediction, Using Electrical Impedance Tomography and Recurrent Neural Networks, *Proceedings of the IEEE-RAS International Conference on Soft Robotics (RoboSoft 2023)*, Singapore, 3–7 April 2023 (IEEE, 2023).
7. L. F. Boesel, D. P. Furundžić, N. Z. Furundžić, A. Gedanken, I. Grabchev, A. Haj Taieb, A. Ivanoksa-Dacik, S. Malionowski, D. Marković, G. Mohr, Y. Oguz Gouillart, P. M. Pinho, A. Sezai Sarac, D. Staneva, S. Tedesco, J. Vincente Ros,
   "Smart textiles for healthcare and medicine applications (WG1): State-of-the art report, CONTEXT Project" (Tech. Rep., European Cooperation in Science and Technology, 2020).
8. M. I. M. Esfahani, M. A. Nussbaum, A "smart" undershirt for tracking upper body motions: Task classification and angle estimation, *IEEE Sensors* **18**, 7650–7658 (2018).
9. Y. Jin, C. M. Glover, H. Cho, O. A. Araromi, M. A. Graule, N. Li, R. J. Wood, C. J. Walsh, Soft sensing shirt for shoulder kinematics estimation. Paper presented at the IEEE International Conference on Robotics and Automation Paris, France, 31 May 2020 to 31 August 2020.
10. M. S. Kim, K. Kim, D. Kwon, S. Kim, J. Gu, Y. S. Oh, I. Park, Microdome-induced strain localization for biaxial strain decoupling toward stretchable and wearable human motion detection. *Langmuir* **36**, 8939–8946 (2020).

11. S. Niu, N. Matsuhisa, L. Beker, J. Li, S. Wang, J. Wang, Y. Jiang, X. Yan, Y. Yun, W. Burnett, A. S. Y. Poon, J. B. Tok, X. Chen, Z. Bao, A wireless body area sensor network based on stretchable passive tags. *Nat. Electron.* **2**, 361–368 (2019).
12. L. M. Castano, A. B. Flatau, Smart fabric sensors and e-textile technologies: A review. *Smart Mater. Struct.* **23**, 053001 (2014).
13. R. S. Saxena, N. K. Saini, R. K. Bhan, Analysis of crosstalk in networked arrays of resistive sensors *IEEE Sensors* **11**, 920–924 (2011).
14. M. Dulal, S. Afroj, J. Ahn, Y. Cho, C. Carr, I. D. Kim, N. Karim, Toward sustainable wearable electronic textiles. *ACS Nano* **16**, 19755–19788 (2022).
15. A. R. Köhler, L. M. Hilty, C. Bakker, Prospective impacts of electronic textiles on recycling and disposal *J. Ind. Ecol.* **15**, 496–511 (2011).
16. M. Nilsson, Tactile sensors and other distributed sensors with minimal wiring complexity *IEEE/ASME Trans. Mechatron.* **5**, 253–257 (2000).
17. A. Tairych, I. A. Anderson, *Electroactive Polymer Actuators and Devices (EAPAD)* (SPIE, 2017), vol. 10163.
18. H. Nesser, G. Lubineau, Achieving super sensitivity in capacitive strain sensing by electrode fragmentation *ACS Appl. Mater. Interfaces* **13**, 36062–36070 (2021).
19. H. Nesser, G. Lubineau, Minimizing the wiring in distributed strain sensing using a capacitive sensor sheet with variable-resistance electrodes *Sci. Rep.* **12**, 13950 (2022).
20. H. A. Sonar, M. C. Yuen, R. Kramer-Bottiglio, J. Paik, An any-resolution pressure localization scheme using a soft capacitive sensor skin. Paper presented at the 2018 IEEE International Conference on Soft Robotics (RoboSoft 2018) Livorno, Italy, 24 to 28 April 2018.
21. D. Xu, A. Tairych, I. A. Anderson, Stretch not flex: Programmable rubber keyboard. *Smart Mater. Struct.***25**, 015012 (2016).
22. J. Lee, S. J. Ihle, G. S. Pellegrino, H. Kim, J. Yea, C.-Y. Jeon, H.-C. Son, C. Jin, D. Eberli, F. Schmid, B. L. Zambrano, A. F. Renz, C. Forró, H. Choi, K.-I. Jang, R. Küng, J. Vörös, Stretchable and suturable fibre sensors for wireless monitoring of connective tissue strain. *Nat. Electron.* **4**, 291–301 (2021).
23. L. Yu, Y. Feng, L. Yao, R. H. Soon, J. C. Yeo, C. T. Lim, Dual-core capacitive microfiber sensor for smart textile applications *ACS Appl. Mater. Interfaces* **11**, 33347–33355 (2019).

24. C. B. Cooper, K. Arutselvan, Y. Liu, D. Armstrong, Y. Lin, M. R. Khan, J. Genzer, M. D. Dickey, Stretchable capacitive sensors of torsion, strain, and touch using double helix liquid metal fibers. *Adv. Funct. Mater.* **27**, 1605630 (2017).
25. Q. Zhang, Y. L. Wang, Y. Xia, P. F. Zhang, T. V. Kirk, X. D. Chen, A low-cost and highly integrated sensing insole for plantar pressure measurement. *Sens. Bio-Sens. Res.* **26**, 100298 (2019).
26. J. Kim, S. Kim, Y. L. Park, Single-input single-output multi-touch soft sensor systems using band-pass filters. *npj Flexible Electron.* **6**, 65 (2022).
27. D. Kim, Y. L. Park, Contact localization and force estimation of soft tactile sensors using artificial intelligence. Paper presented at the IEEE International Conference on Intelligent Robots and Systems, Madrid, Spain, 1 to 5 December 2018.
28. K. K. Kim, M. Kim, K. Pyun, J. Kim, J. Min, S. Koh, S. E. Root, J. Kim, B. N. T. Nguyen, Y. Nishio, S. Han, J. Choi, C. Y. Kim, J. B. Tok, S. Jo, S. H. Ko, Z. Bao, A substrate-less nanomesh receptor with meta-learning for rapid hand task recognition. *Nat. Electron.* **6**, 64 (2022).
29. M. Cao, J. Su, S. Fan, H. Qiu, D. Su, L. Li, Wearable piezoresistive pressure sensors based on 3D graphene. *Chem. Eng J.* **406**, 126777 (2021).
30. X. Li, X. Li, T. liu, Y. Lu, C. Shang, X. Ding, J. Zhang, Y. Feng, F. J. Xu, Wearable, washable, and highly sensitive piezoresistive pressure sensor based on a 3D sponge network for real-time monitoring human body activities. *ACS Appl. Mater. Interfaces.* **13**, 46848 (2021).
31. Y. A. Lin, Y. Zhao, L. Wang, Y. Park, Y. J. Yeh, W. H. Chiang, K. J. Loh, Graphene K-Tape meshes for densely distributed human motion monitoring. *Adv. Mater. Technol.* **6** (2021).
32. T. J. Cuthbert, B. C. Hannigan, A. Shokurov, C. Menon, HACS: Helical auxetic yarn capacitive strain sensors with sensitivity beyond the theoretical limit. *Adv. Mater.* **35** 2209321 (2023).
33. M. Amjadi, K. U. Kyung, I. Park, M. Sitti, Stretchable, skin-mountable, and wearable strain sensors and their potential applications: A review *Adv. Funct. Mater.* **26**, 1678–1698 (2016).
34. A. Tairych, I. A. Anderson, *Proceedings of SPIE, Electroactive Polymer Actuators and Devices (EAPAD*) (no. 10594, SPIE, 2018).
35. A. Tairych, I. A. Anderson, A numerical method for measuring capacitive soft sensors through one channel. *Smart Mater. Struct.* **27**, 035016 (2018).
36. R. Bellman, K. J. Åström, On structural identifiability *Math. Biosci.* **7**, 329–339 (1970).
37. M. N. Chatzis, E. N. Chatzi, A. W. Smyth, On the observability and identifiability of nonlinear structural and mechanical systems. *Struct. Control Health Monit.* **22**, 574–593 (2015).

38. C. Hwang, B. Nakano, T. Asahi, Transformation of state-space model to Cauer I and II CFE canonical forms *Int. J. Syst. Sci.* **15**, 797–804 (1984).
39. G. Calzavara, L. Consolini, J. Kavaja, Structured identification for network reconstruction of RC-models. *Systems and Control Letters* **147**, 104849 (2021).
40. L. Ljung, On convexification of system identification criteria. *Autom. Remote Control* **80**, 1591–1606 (2019).
41. E. L. White, M. C. Yuen, R. K. Kramer, *2017 IEEE Sensors* (IEEE, 2017).
42. A. Rezaei, T. J. Cuthbert, M. Gholami, C. Menon, Application-based production and testing of a core–sheath fiber strain sensor for wearable electronics: Feasibility study of using the sensors in measuring tri-axial trunk motion angles. *Sensors* **19**, 4288 (2019).
43. B. C. Hannigan, T. J. Cuthbert, W. Geng, C. Menon, Understanding the impact of machine learning models on the performance of different flexible strain sensor modalities. *Front. Mater.* **8**, 44 (2021).
44. A. Hamed, E. Tisserand, Y. Berviller, V. Nancy, Fast FPGA implementation of an original impedance analyser. *Sens. Transducers* **10**, 191–205 (2011).
45. R. Kusche, A. Malhotra, M. Ryschka, G. Ardelt, P. Klimach, S. Kaufmann, A FPGA-Based Broadband EIT system for complex bioimpedance measurements—Design and performance estimation *Electron.* **4**, 507–525 (2015).
46. R. Schreier, G. C. Temes, *Understanding Delta-Sigma Data Converters* (Wiley, 1997), vol. 53 .
47. L. Risbo, *Sigma Delta Modulators - Stability Analysis and Optimization*, (Doctor of Philosophy, Technical University of Denmark, 1994).
48. B. C. Hannigan, C. L. Petersen, A. M. Mallinson, G. A. Dumont, An optimization framework for the design of noise shaping loop filters with improved stability properties*, Circuits Syst. Signal Process.* **39**, 6276–6298 (2020).
49. A. Behrouzirad, P. Sugrue, M. Todorovic, K. G. McCarthy, P. Galvin, *2021 32nd Irish Signals and Systems Conference* (ISSC, 2021).
50. A. Klein, W. Schumacher, Algebraic operations on delta-sigma bit-streams *Math. Comput. Appl.* **23**, 49 (2018).
51. D. G. Zrilic, *Functional Processing of Delta-Sigma Bit-Stream* (Springer, 2020).
52. J. Jeong, N. Collins, M. P. Flynn, A 260 MHz IF sampling bit-stream processing digital beamformer with an integrated array of continuous-time band-pass modulators *IEEE J. Solid-State Circuits* **51**, 1168–1176 (2016).

53. E. Hogenauer, An economical class of digital filters for decimation and interpolation. *IEEE Trans. Signal Process.* **29**, 155–162 (1981).
54. K. Tindell, “Microcontroller interconnect network (MIN) protocol”; https://github.com/min-protocol/min/wiki.
55. C. Wolf, M. Lasser, “Project IceStorm”; http://bygone.clairexen.net/icestorm/.
56. K. J. Keesman, *System Identification - An Introduction* (Springer-Verlag, 2011).
57. H. Hong, A. Ovchinnikov, G. Pogudin, C. Yap, SIAN: Software for structural identifiability analysis of ODE models. *Bioinformatics* **35**, 2873–2874 (2019).
58. N. Mart’ınez, A. F. Villaverde, Nonlinear observability algorithms with known and unknown inputs: Analysis and implementation. *Mathematics* **8**, 1 (2020).
59. E. August, Parameter identifiability and optimal experimental design. Paper presented at the 2009 International Conference on Computational Science and Engineering, Vancouver, Canada, 29 to 31 August 2009
60. A. F. Villaverde, N. D. Evans, M. J. Chappell, J. R. Banga, Input-dependent structural identifiability of nonlinear systems. *IEEE Control Syst. Lett.* **3**, 272–277 (2019).
61. J. Karlsson, M. Anguelova, M. Jirstrand, An efficient method for structural identifiability analysis of large dynamic systems, *IFAC* **45** 941–946 (2012).